# Strain partitioning across a subduction thrust fault near the deformation front of the Hikurangi subduction margin, New Zealand: A magnetic fabric study on IODP Expedition 375 Site U1518

Annika Greve [a],[*],[1], Myriam Kars [b], Lilly Zerbst [c], Michael Stipp [d], Yoshitaka Hashimoto [e]

[a] *Institute for Marine-Earth Exploration and Engineering, Japan Agency for Marine-Earth Science and Technology, Yokosuka, Japan*
[b] *Center for Advanced Marine Core Research, Kochi University, Nankoku, Japan*
[c] *Geophysical Institute, Karlsruhe Institute of Technology, Karlsruhe, Germany*
[d] *Institute of Geosciences and Geography, Martin-Luther University, Halle, Germany*
[e] *Department of Global Environment and Disaster Prevention, Faculty of Science and Technology, Kochi University, Japan*

## ARTICLE INFO

## ABSTRACT

Understanding the distribution of strain along thrust and splay faults in active accretionary systems is crucial to understand the mechanical properties of the sediments and the strength of the fault zone and its slip behavior. This paper investigates the distribution of strain through sediment compaction and texture development across the Pāpaku fault, a major splay fault near the deformation front of the Hikurangi subduction margin, New Zealand using the anisotropy of magnetic susceptibility technique (AMS). International Ocean Discovery Program Site U1518 penetrated hanging wall, fault zone and footwall sequences to a maximum depth of 484.9 meters below seafloor. A total of 330 discrete samples was subjected to AMS measurements and magnetic remanence data used to reconstruct the axial orientation of each sample in a geographic reference frame. The AMS display distinct fabric differences between hanging wall, through the fault zone and footwall domains, demonstrating that strain is partitioned across the fault zone. Hanging wall sequences show a strike-parallel northeasterly lineation of $K_{max}$ and weakly prolate shapes, typical for a component of northeast-southwest lateral shortening. In contrast, footwall sequences are more oblate and show a clustering of $K_{max}$ in northerly direction. This demonstrates that strain in the footwall is dominated by gravitational loading, however a component of sub-horizontal east-westerly strain, parallel to the convergence direction of the Pacific Plate exists. Strain decoupling between hanging- and footwall sequences occurs near the top of the Pāpaku fault zone. Differences in the degree of magnetic susceptibility between footwall sediments incorporated into the fault zone, and the underlying undeformed footwall sequences are indicative for the progressive dewatering of the underconsolidated footwall sequences.

© 2020 The Author(s). Published by Elsevier B.V. This is an open access article under the CC BY license (http://creativecommons.org/licenses/by/4.0/).

## 1. Introduction

Subduction earthquakes and tsunami pose a significant hazard to coastal communities around the Pacific (e.g. Moore et al., 2011). Seismological and geodetic information have established that subduction zones host a range of slip styles, including destructive megathrust- and tsunami earthquakes, but also aseismic slow-slip earthquakes (e.g. Fagereng et al., 2019; Wallace et al., 2016). The interrelation between non-destructive earthquakes,

stress build-up and release is not fully understood yet. In particular it is not known what role splay- and shallow subduction thrust faults play in the propagation and release of seismic energy. For instance, while a recent seafloor geodetic study (Wallace et al., 2016) demonstrated that slow-slip earthquakes can propagate all the way to the trench, it is yet unclear whether they occur within the shallowest parts of the accretionary system.

Key to understanding the slip behavior is to understand how stress and strain are distributed across shallow thrust faults (e.g. Stipp et al., 2013; Kuehn et al., 2019b). Studies that aim to reconstruct type and distribution of strain within accretionary prisms often overlook the effect of ductile strain and texture development in the soft sediments. This is particularly significant close to the trench, where the soft and porous sediments of the incoming plate are accreted, tectonically deformed, compacted and
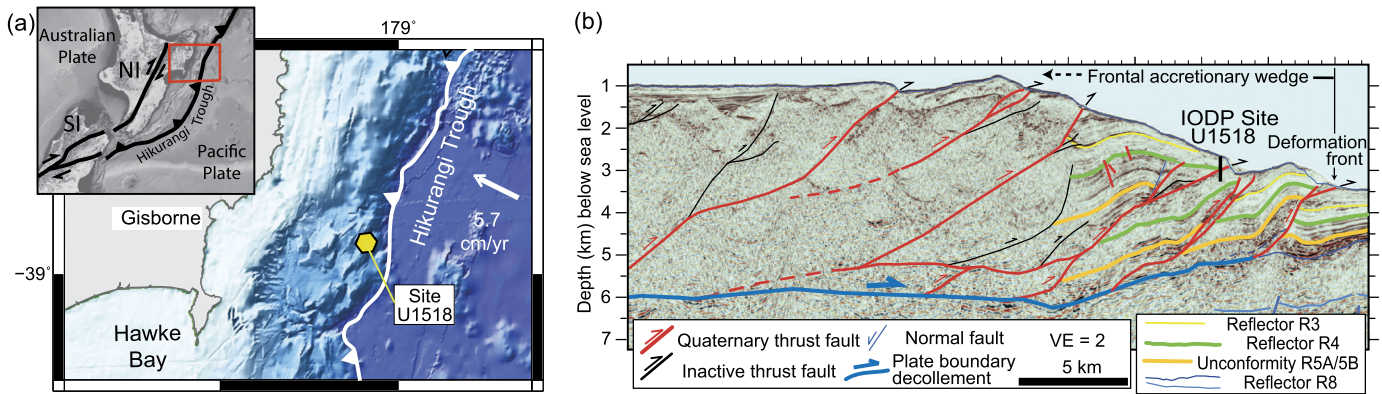
**Fig. 1.** Tectonic setting of the study area. (a) General overview of the northern Hikurangi subduction margin and the New Zealand plate boundary zone (inset), bathymetric map of the northern Hikurangi subduction margin, main thrust faults, and the location of IODP Site U1518. Also displayed is the relative plate convergence vector. (b) Simplified interpretation of a seismic cross section of the frontal accretionary wedge near the drilling transect of IODP Expedition 375. Modified from Fagereng et al. (2019), seismic velocity model of Barker et al. (2018). (For interpretation of the colors in the figure(s), the reader is referred to the web version of this article.)

dewatered. During these processes, grains with a shape anisotropy in the mostly clay-rich sediments tend to rotate from an initial, usually bedding parallel fabric alignment towards an alignment predominantly of face-to-face contacts perpendicular to the principal shortening direction (Kanamatsu et al., 2012; Parés, 2015; Kuehn et al., 2019b). The sediment fabrics yield information about the tectonic deformation regime during early accretion in a three-dimensional reference frame. It also controls the physical and hydrological properties of the sediment and consequently seismogenic behavior (Morgan et al., 2007).

One possible explanation why the localization and partitioning of strain across subduction thrust faults is not fully understood yet is that widespread ductile deformation processes are difficult to observe and quantify. Anisotropy of magnetic susceptibility (AMS) arises from the preferential alignment of minerals, which is often dominated by the clay minerals in sediments. The AMS tensor effectively measures the eccentricity of shape of the magnetic ellipsoid from which the directions and distribution of three principal axes of magnetic susceptibility can be determined ($K_{max} > K_{int} > K_{min}$). These can help to define the degree, type and direction of weak strain in sediments (see for example Parés, 2015). AMS studies have successfully been applied to understand the distribution and direction of strain in modern (Housen et al., 1996; Housen and Kanamatsu, 2003; Yang et al., 2013; Ujiie et al., 2003; Kitamura et al., 2010) and extinct (Kanamatsu et al., 1996, 2001, 2012) accretionary systems, and in fold and thrust belts (e.g. Kuehn et al., 2019a).

In this study we use the AMS method as proxy for strain at Site U1518 of International Ocean Discovery Program (IODP) Expedition 375 in a three-dimensional geographic reference frame. This site sampled the Pāpaku fault, a shallow and active thrust fault near the deformation front of the Hikurangi subduction margin (New Zealand). A more detailed picture of the distribution and decoupling of strain in the fault zone will improve our understanding of what role shallow subduction thrusts faults play in the evolution of young accretionary prisms.

## 2. Geology

The Hikurangi margin is the site of oblique convergence between the Pacific and Australian Plates. It is located offshore the eastern coast of the Central North Island in New Zealand (Fig. 1a). The relative convergence rates between the Pacific and Australian plates decreases from 48 mm/yr in the North to 43 mm/yr in the South, where the plate boundary zone transforms into transpressional with the most prominent Alpine Fault along the South Island

of New Zealand (Fig. 1a; Wallace et al., 2004). IODP Expedition 375 Site U1518 targeted the Pāpaku fault, a major frontal thrust, ca. 6.5 km from the deformation front of the northern Hikurangi margin (Wallace et al., 2019; Barker et al., 2018, Fig. 1b). At this site, the accretionary system is largely tectonically erosional and characterized by an over-steepened frontal slope. Geodetic instrumentation showed that at this site, the plate interface is subjected to periodic creep (e.g. Wallace et al., 2016). There is also evidence for a range of seismic styles in the past, including two tsunamiproducing earthquakes which occurred in 1947 (Barker et al., 2018; Bell et al., 2014).

IODP Expedition 375 recovered sediments from the incoming plate and accretionary sequences on the overriding plate of the Hikurangi subduction margin, with the aim to better understand the material properties and mechanics that govern a range of seismic and slip styles found at this plate interface. Site U1518 penetrated a shallow thrust fault within the hanging wall of the accretionary prism, in a region which is known to host both tsunamiproducing and slow-slip earthquakes (e.g. Fagereng et al., 2019; Wallace et al., 2016, 2019; Barker et al., 2018). Drill-cores were recovered from two holes. Hole U1518E penetrated sediments between the seafloor and 175.6 meters below seafloor (mbsf) using the Advanced Piston Coring (APC) and Extended Core Barrel (XCB) coring systems. Hole U1518F penetrated sediments between 197.7 and 484.9 mbsf using the Rotary Core Barrel (RCB) system. Additional logging-while drilling (LWD) datasets were recovered during precursor IODP Expedition 372 from Holes U1518A (0-117.8 mbf) and Holes U1518B (ca. 50-600 mbsf), both of which are located within 35 m from Holes U1518E and U1518F. The lithology throughout the recovered sequence consists of Pleistocene silty-clays and muds that alternate with coarser silt and sand- (turbidite) beds. Lithologic unit classifications are largely based on the frequency of turbidite deposits and will not be further discussed in this paper (Wallace et al., 2019). Three major structural domains of the Pāpaku fault were sampled. The hanging wall (0-304 mbsf) shows signs of internal folding with intact bedding and localized zones of pervasive fracturing. At ca. 300 mbsf Holes U1518B and U1518F penetrate the top of the fault zone. The boundary between hanging wall and fault zone is marked by a sharp transition from coherent bedding, to pervasively brittlely and ductilely deformed fault zone rock (Fagereng et al., 2019). The deformation style is localized and variable. In many cases, brittle features such as fracturing and brecciation overprint zones of pervasive ductile shearing and flow banding. Most of the deformation is localized within two strands, which were defined as a "main brittle fault zone" between 304.5 and 322.4 mbsf, and a "subsidiary fault zone"

between 351.2-361.7 mbsf (Wallace et al., 2019). The intervening zone (322.4-351.2 mbsf) has experienced lower intensity deformation and intact bedding remained in localized zones (Wallace et al., 2019).

Biostratigraphic observations identified an age inversion near the top of the fault zone, suggesting that hanging wall sediments are older and fault- and footwall sediments younger than 0.53 Ma (Wallace et al., 2019). This is supported by a transition from bedding which predominantly tilts in northeast (NE) – southwest (SW) direction in the hanging wall, to shallow (tilt angle 10-20°) northerly (N) to northwesterly (NW) directed bedding tilts which predominate both fault zone and footwall. The footwall, which in this setting remains situated within the hanging wall of the accretionary system is tectonically largely undeformed. Some domains with visible distortion and flow structure were interpreted as gravity driven mass transport deposits. These distorted domains are interbedded with intervals of intact strata, the latter of which were sampled for this study (Wallace et al., 2019).

## 3. Methods

A total of 330 oriented cube samples were collected from working-half sections by pushing 7 cm$^3$ plastic cubes into the sediment (refer to Wallace et al., 2019 for sampling methods). Visible core-disturbance, mass transport deposits or localized deformation features were avoided during sampling. AMS measurements were conducted using an AGICO (Type KLY-4) Kappa Bridge at the Japan Agency for Marine-Earth Science and Technology (JAMSTEC) in Yokosuka, Kanagawa, Japan. Subsequently the samples were subjected to stepwise Alternating Field (AF) demagnetization along 3-axes up to 80 mT using a horizontal 2-G SQUID passthrough cryogenic magnetometer which is equipped with an in-line degausser. The corrected degree of magnetic anisotropy Pj, the shape factor T, for which values T > 0 suggest oblate and T < 0 prolate shaped fabrics, and the inclinations of the three principal axes of magnetic susceptibility, $K_{min}$, $K_{int}$ and $K_{max}$ were calculated from the principal susceptibilities ($K_{max} > K_{int} > K_{min}$) (Jelinek, 1981). Due to the absence of continuous bedding markers or other features that would allow to re-orient core-material with the aid of resistivity logs, remanence directions were used to restore the orientation of core-material. The re-orientation procedure assumes that the recovered sediments acquired their remanence in a geocentric axial dipole (GAD) field, and the sample declination measurements were used to determine the orientation of each individual sample in respect to geographic North (see for example Kanamatsu et al., 2012). Averaged over long time-scales Earth's magnetic field resembles that of a GAD. It is noteworthy however that each individual sample produces a spot reading of the ambient magnetic field at the time the sample remanence was acquired. Secular variation records for the last 15,000 years in New Zealand describe swings in declination that range in their extremes from 33.5° W to 26.0° E (Greve and Turner, 2017). While the scale of secular variation in New Zealand further back in time is not well known, this provides a first order constraint on the orientation inaccuracy to be expected. Further error may be introduced during determination of characteristic remanence directions: Specimens usually showed demagnetization trajectories that were affected by pervasive drilling induced overprints in the coercivity range from 0-15 mT. Further, treatment with a static alternating field of 35 mT or more usually resulted in the acquisition of a strong gyroremanence (see for example Hu et al., 2002; Wallace et al., 2019). Straight-line demagnetization trajectories towards the origin were usually identifiable only in a narrow interval between 20 and 30 mT. To avoid systematic biases caused by gyroremanence acquisition, we thus opted to use the remanence declinations measured at the 20 mT demagnetization step. This approach can introduce a significant

error, in particular in samples that carry multiple component remanences. In this case, any primary remanence carrier was probably entirely replaced by diagenetically formed iron-sulfide minerals (e.g. greigite, section 4.1) and the use of a single demagnetization step following removal of drilling induced overprints considered the most reliable approach. Further discussion of these demagnetization results will also be detailed in a future contribution. To aid the identification of the magnetic minerals, and to identify whether any downhole trends in the rock magnetic properties affected the interpretation of the AMS data, further rock magnetic experiments were conducted on a smaller number of samples at the Center for Advanced Marine Core Research, Kochi University (Nankoku, Kochi, Japan). After initial AF demagnetization of the natural remanent magnetization (NRM), anhysteretic remanent magnetization (ARM) was imparted in a direct current bias field of 50 μT and a peak alternating field of 80 mT. Selected samples were subjected to stepwise partial ARM (pARM) acquisition (with an alternating field from 5 to 80 mT). Hysteresis properties (saturation magnetization $M_s$, saturation remanent magnetization $M_{rs}$, coercivity $B_c$ and remanent coercivity $B_{cr}$) were measured on dry powder samples at room temperature using a Princeton Measurements Corporation vibrating sample magnetometer (VSM) with a 1 T saturating field. First-order reversal curves (FORCs, Pike et al., 1999) were measured on evenly spaced samples (every ∼10 m stratigraphic interval wherever possible, averaging time: 100 ms, field increment: 2 mT, number of FORCs: 150, $B_u$ from -60 to 60 mT and $B_c$ up to 150 mT). FORC diagrams were processed using the FORCinel software (Harrison and Feinberg, 2008).

## 4. Results

### 4.1. Magnetic mineralogy

AMS measures the bulk fabric of dia-, para- and ferromagnetic minerals in a sample and it is difficult to assess the contributions of different mineral phases to the bulk signal. It is thus important to understand the presence of paramagnetic fabric, as well as the grain-size, composition and distribution of ferromagnetic minerals in a sample. Downhole rock magnetic parameters, including magnetic susceptibility and natural remanent magnetization (NRM) are displayed in Fig. 2 together with five AMS Units that we define below.

The natural remanence (NRM) and magnetic susceptibility show little variation throughout Site U1518. NRM intensities are about 0.001 A/m (Fig. 2c) and the bulk susceptibility is low and ranges from 1 to 2 x 10$^{-4}$ SI (Fig. 2c). With few exceptions, and an interval below 460 mbsf, all samples from AMS Units II, III, IV and V (197.7 to 494.9 mbsf) yield coercivities ($B_c$) in the range of 50 mT (Kars et al., 2019). In AMS Unit I (0 to 156 mbsf), the coercivity alternates in intervals between values around 20 mT and higher values around 50 mT (Kars et al., 2019). Representative hysteresis, FORC and ARM acquisition curves for high coercivity and low coercivity samples are displayed in Fig. 3. FORC diagrams of high coercivity intervals (Fig. 3a) are characterized by closed contours with a mean coercivity of ∼60 mT and pARM acquisition curves show a wide distribution of coercivity, with all of the samples being dominated by magnetic mineral phases with coercivities of 30 mT or more. This signature is typical for samples that contain single domain (SD) greigite as remanence carrier (Roberts et al., 2006). Common occurrence of greigite throughout Site U1518 samples was inferred from shipboard measurements which showed gyroremanence (GRM) acquisition (Wallace et al., 2019). For low coercivity samples, the FORC diagrams have contour lines with a triangular shape and a mean coercivity < 20 mT with a tail up to 100 mT. We suggest that these diagrams are caused by the presence of single domain (SD) to multidomain (MD) sized low
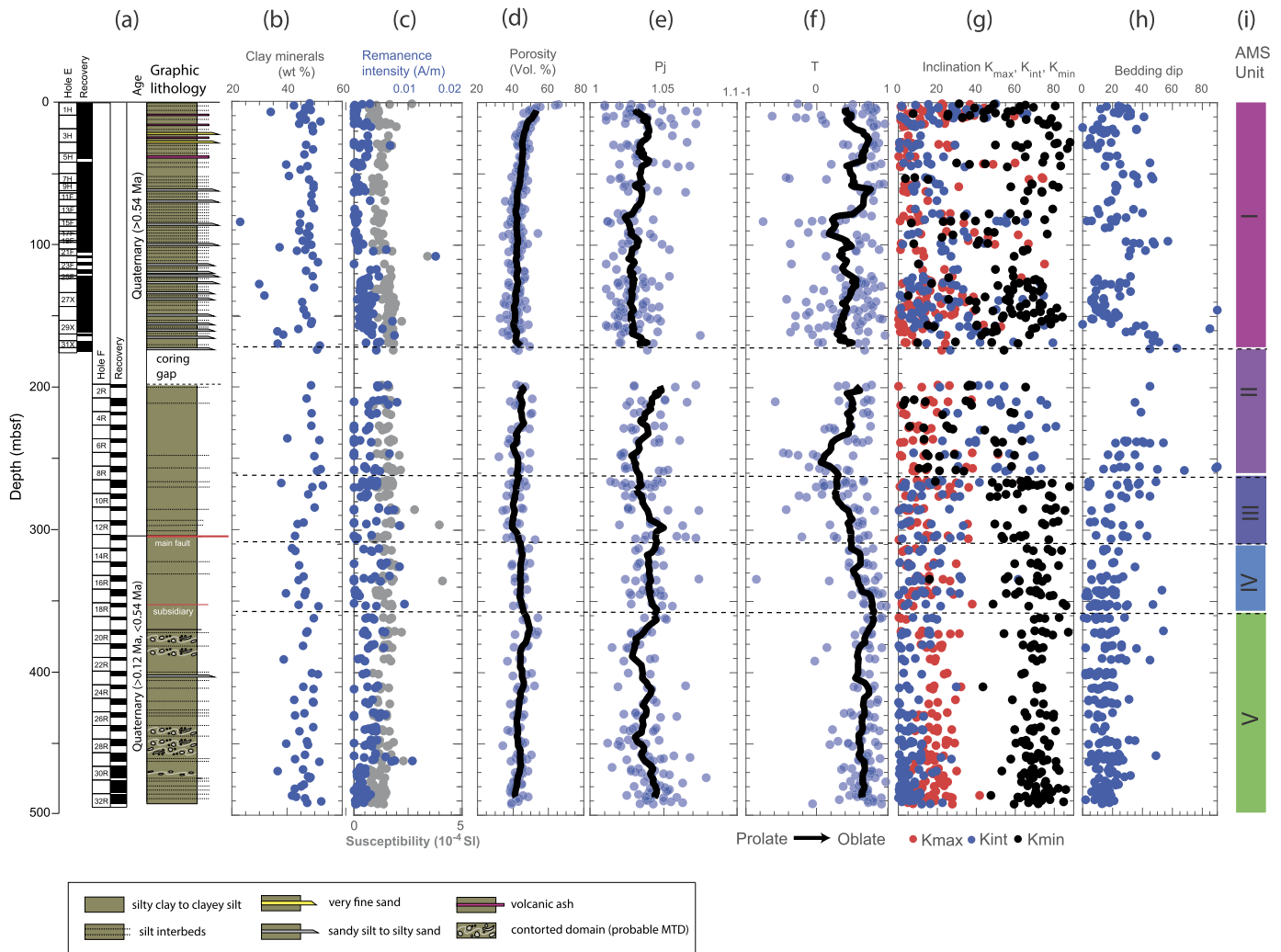
**Fig. 2.** Down-core profiles of (a) lithology, (b) concentration of clay minerals in the bulk sediment, (c) remanence intensity (blue) and mean magnetic susceptibility measured for each individual sample (gray), (d) porosity, (e) corrected degree of anisotropy (Pj), (f) the magnetic shape factor (T), (g) inclination of the three principal axes of AMS, (h) bedding dips recorded on axially unoriented core-material, (i) AMS units defined in this paper. In Figure (d-f) we also display the running average, calculated in one meter increments and including all datasets within ten meter segments, for each AMS Unit respectively (black line). For a description of the datasets recorded in a, b, d and h refer to Wallace et al. (2019).

coercivity magnetic mineral phases (likely (Ti-)magnetite) (Mux-worthy and Dunlop, 2002; Roberts et al., 2000), although it can not be precluded that SD greigite is present as well.

Comparison between the high-field susceptibility or high-field slope in hysteresis curves with the low-field, or mean susceptibility ($K_m$) measured on discrete cube samples allows to estimate the total contribution of ferromagnetic minerals to the bulk magnetic susceptibility. Prior to slope correction, hysteresis loops are dominated by a strong linear trend (Fig. 3), and paramagnetic minerals dominate the signal. Our calculations showed that in AMS Units II, III and IV, V the high-field susceptibility differs by ca. ± 15% from the bulk susceptibility. Somewhat larger differences of up to ± 50% were measured on some samples from AMS Unit I. Differences in the sample size used (2 x 2 cm cube vs. capsule for VSM measurements), fabric alignment in the discrete cube samples and instrument used may contribute to differences in the calculation of the net contribution of ferromagnetic minerals in samples. Nevertheless the results demonstrate that although the ferromagnetic minerals are contributing to the mean susceptibility, the magnetic susceptibility is dominated by paramagnetic minerals. These observations are also supported by bulk powder XRD analyses (Wallace et al., 2019) which found that the clay mineral content (smectite + illite + chlorite + kaolinite) ranges from ca. 35-53% throughout

the recovered sequence and averages to ~45% (Fig. 2b). The low susceptibilities and the total clay mineral content fall well into the range expected for a mudstone, for which the susceptibility measured is often dominated by paramagnetic fabric (e.g. Parés, 2015).

### 4.2. AMS and AMS Unit classification

Throughout most of the sequence the AMS ellipsoids yield low to moderate degrees of anisotropy (Pj) that range from 1.01 to 1.08, and the shape factor (T) predominantly yields positive values, which indicates predominantly oblate shapes. The down-core distribution of the corrected degree of anisotropy (Pj) and T, and the inclinations of the principal axes of magnetic susceptibility, together with bedding tilt data and the shipboard core-description allows to define five distinct AMS units that largely coincide with the main structural domains, including the hanging wall, fault zone and footwall (Figures 2 and 4; Wallace et al., 2019).

#### 4.2.1. Hanging wall (AMS Units I, II, III)

We subdivide the hanging wall into three AMS Units. AMS Unit I (0-156 mbsf) forms the upper hanging wall and is dominated by gentle, NE bedding tilts that range from ca. 10° to 45°. In this unit, $K_{min}$ dominantly yields vertical (or steep) inclinations, while $K_{max}$
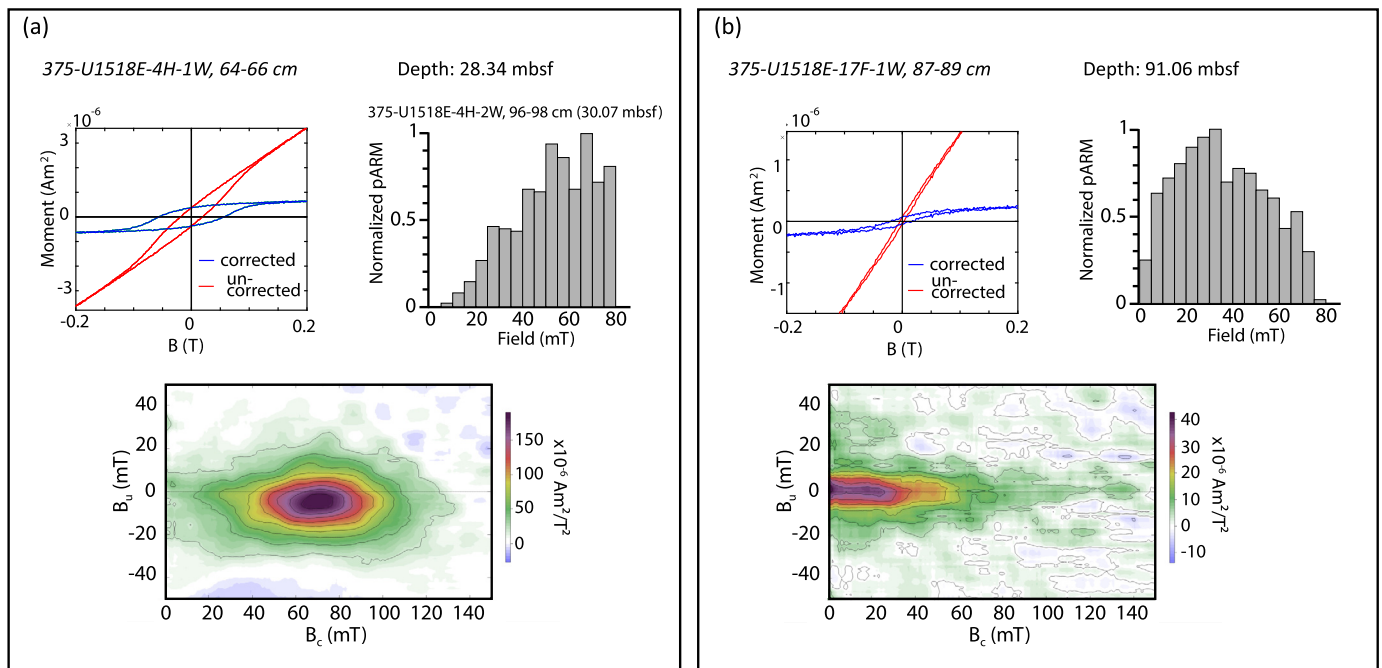
**Fig. 3.** Representative rock magnetic results for (a) the predominant, high-coercivity intervals in AMS Units I, II, III, IV, V and (b) isolated low coercivity intervals within AMS Units I and V. Displayed are magnetic hysteresis loops prior to and following slope correction (left), pARM acquisition (right) and FORC diagrams (bottom). See text for details.

and $K_{int}$ yield shallow inclinations in the range of 5° to 20°. Some variation is likely related to disturbance of the soft and unconsolidated sediment in this unit during the recovery of piston cores (for a discussion of drilling disturbance in piston cores refer to Snowball et al., 2019; Wallace et al., 2019). At 156 mbsf, the baseline of Pj increases from ca. 1.017 to 1.02 and we define this as the boundary between AMS Units I and II. Between 175.6 and 197.9 mbsf is a coring gap. The mid hanging wall (AMS Unit II) is characterized by steep bedding tilts (ca. 35-60°) in NE and SW direction with localized zones of overturned bedding (Wallace et al., 2019). In this unit, the inclinations of $K_{min}$ and $K_{int}$ are distributed more widely. At ca. 275 mbsf, there is a major fold-hinge zone that is characterized by fractured and pervasively deformed fold limbs (Wallace et al., 2019). Within this zone the shape factor T of the AMS ellipsoids measured indicates triaxial to prolate magnetic fabrics. Here we define the boundary to the lower hanging wall, or AMS Unit III (275-304 mbsf), in which beds tilt moderately (ca. 15-40°) in NE direction and the inclinations of the three principal axes of susceptibility are similar to those of AMS Unit I, where $K_{min}$ tilts steeply, while $K_{max}$ and $K_{int}$ are close to horizontal (ca. 0-30°).

Re-orientation of the AMS tensors allows to compare the directional distribution of the three principal axes of magnetic susceptibility. Throughout the hanging wall $K_{max}$ cluster in NW and SE direction. In AMS Unit I $K_{max}$ and $K_{int}$ fall are distributed about the bedding plane, while $K_{min}$ is perpendicular to bedding. In AMS Units II and III the $K_{min}$ axes form a girdle around $K_{max}$ (Fig. 4). Here it is noteworthy that the re-orientation of the AMS ellipsoids within AMS Unit II is subjected to higher uncertainty due to the steeper bedding tilts. Further, variable or overturned bedding in NE and SW direction would have resulted in a fold axis perpendicular dispersion of the $K_{min}$ directions in this unit.

*4.2.2. Fault zone (AMS Unit IV)*

We define the boundary between AMS Units III and IV to coincide with the upper strand of the Pāpaku fault (Fagereng et al., 2019) at 304 mbsf. The baseline in Pj in the fault zone is with 1.04 only slightly higher than in AMS Units II and III, but within the fault zone it shows a wide dispersion with values ranging from

1.02 to 1.08 (Figs. 2, 4, 5) and shape parameters indicating mostly oblate but also some prolate shapes. A direct correlation between the degree of anisotropy and the presence of mesoscopically visible deformation features within the main brittle and lower subsidiary fault zone is not apparent (Fig. 4, 5). Bedding tilt data recovered within the 60 m thick fault zone indicate gentle (ca. 10-15°) NW tilts. Following re-orientation, the principal axes of susceptibility indicate, on average, a bedding parallel foliation, where $K_{min}$ is perpendicular to bedding, while $K_{int}$ and $K_{max}$ fall into the bedding plane. However, while the upper strand of the Pāpaku fault displays $K_{max}$ directions that predominantly fall in SW direction, the intervening, weakly deformed zone (322.4-351.2 mbsf) displays a northward (N) lineation, similar to the footwall (AMS Unit V, section 4.2.3; Fig. 5).

*4.2.3. Footwall (AMS Unit V)*

The top of the footwall at 361 mbsf (AMS Unit V) is marked by an increase in the porosity from ca. 45% to ca. 50% (Wallace et al., 2019, Figure 2d). At this boundary the value of Pj decreases sharply from ~1.04 to ~1.018 and subsequently increases with depth. Footwall sediments dip gently N and show only minor visible deformation (Wallace et al., 2019). In contrast to hanging wall sediments, AMS measurements on the footwall sediments display a foliation dominated fabric, in which $K_{max}$ and $K_{int}$ display similar values, while $K_{min}$ is clearly distinct. Following re-orientation, $K_{max}$ forms a cluster in N-direction.

**5. Discussion**

*5.1. Strain partitioning between hanging- and footwall sequences of the Pāpaku fault*

The AMS data discussed in this paper are largely coherent with structural observations and porosity measurements made on core-material (Wallace et al., 2019; Fagereng et al., 2019). Common observations include: (i) a bedding parallel magnetic foliation throughout most of the sequence, (ii) the predominance of more extensively deformed, prolate-type fabrics in the region of a major
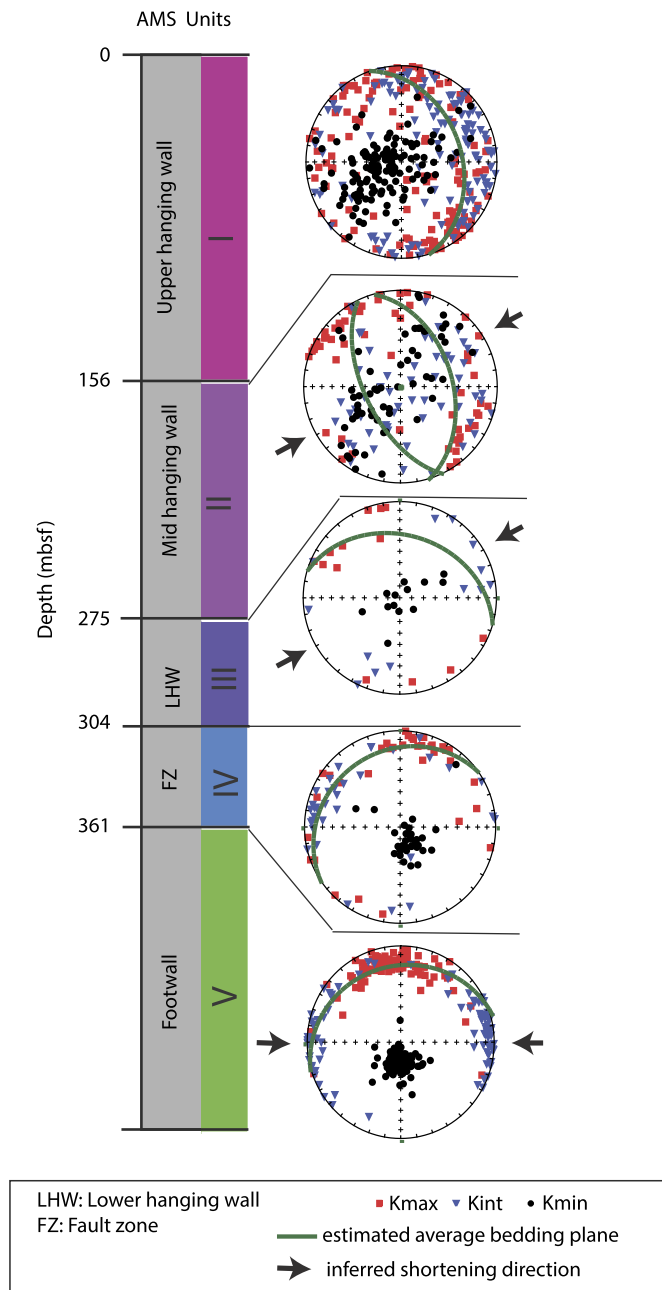
**Fig. 4.** AMS Units and lower hemisphere projections for the principal axes of magnetic susceptibility, approximate bedding plane(s) estimated for each unit from the shipboard interpretations of downhole resistivity image logs (center) (Wallace et al., 2019).

tal contribution is subject to composition, quantity, orientation and magnetic grain-size of the ferromagnetic minerals in each sample (see for example Aubourg and Robion, 2002). Rock magnetic measurements (Kars et al., 2019) display a largely coherent signature that is characteristic for the presence of SD-sized greigite through AMS Units II, III, IV and Unit V (above 460 mbsf), and we suggest that the sudden differences in the orientation of the principal axes of susceptibility between neighboring AMS Units likely reflect on differences in the depositional and deformation regime. In contrast, a larger scatter found within AMS Unit I (Fig. 2) may be associated to variable contributions of ferromagnetic minerals to the magnetic susceptibility measured. Previous studies have demonstrated that in horizontally settled, clay-rich sediment the AMS tensor tends to display bedding parallel oblate ellipsoids in which the $K_{min}$ axes cluster in a direction that is perpendicular to bedding. Directed sediment flow, for example in mass-transport deposits or turbidite systems, can result in an imbrication of the $K_{min}$ directions from a bedding perpendicular orientation (e.g. Novak et al., 2014). Although we avoided gravity driven deposits during sampling, such depositional processes may have affected the magnetic fabric of some samples. Increased horizontal loading and dewatering through burial further increases the degree of anisotropy, which is a function of the ratio between $K_{max}$ and $K_{min}$ (Parés, 2015). If a sediment undergoes multiple and successive deformation processes, the clay minerals tend to begin to align in an angle to the bedding plane, resulting on average, in a magnetic lineation fabric with $K_{max}$ aligning with the intersection of the two planes that are perpendicular to the direction of maximum compressive strain (Hirt et al., 2004; Graham, 1966) or parallel to the stretching direction in an extensional setting (Cifelli et al., 2004). In addition to the determination of the three-dimensional strain, the joint analysis of AMS datasets with small-scale, localized brittle-ductile deformation features can be used to better understand the distribution of strain (e.g. Housen et al., 1996).

The AMS fabric described in this paper demonstrate a distinct difference of the deformation character and orientation of the principal strain axes between hanging wall, through the fault zone and footwall of the Pāpaku fault. It is remarkably similar to the strain distribution found across the décollements of the Japan Trench system (Yang et al., 2013), the Nankai accretionary prism offshore Muroto (Ujiie et al., 2003; Owens, 1993; Taira et al., 1992) and the Barbados accretionary margin (Housen et al., 1996). In all three settings, the authors describe fabric that depicts trench-perpendicular sub-horizontal shortening within the accretionary prism (here: hanging wall), which is decoupled by a strongly deformed décollement zone from weakly to moderately deformed, mostly underthrust sediments that are characterized by oblate shaped deformation ellipsoids in which $K_{max}$ and $K_{int}$ are distributed randomly in the bedding plane. Similarly, hanging wall sediments at IODP Site U1518 show a roughly strike-parallel, NW-SE lineation of $K_{max}$, in which horizontal shortening through texture development occurred simultaneously with tilting. While the AMS ellipsoids of the hanging wall sediments are weakly prolate and core-descriptions also identified folding and locally pervasive fracturing in this domain, the sediments of the footwall are largely undeformed (Wallace et al., 2019) and clearly dominated by a sub-horizontal, oblate magnetic fabric. In contrast to AMS and fabric studies from the Nankai, Tohoku and Barbados accretionary systems however (Morgan and Karig, 1995; Housen et al., 1996; Yang et al., 2013; Ujiie et al., 2003; Owens, 1993), the $K_{max}$ directions of footwall sequences form a cluster in dip (N) direction. From these AMS results we infer that although gravitational loading dominates the fabric development in the footwall, a component of sub-horizontal strain in E-W direction exists, probably in response to further deformation within the accretionary sequence sampled below the Pāpaku fault.
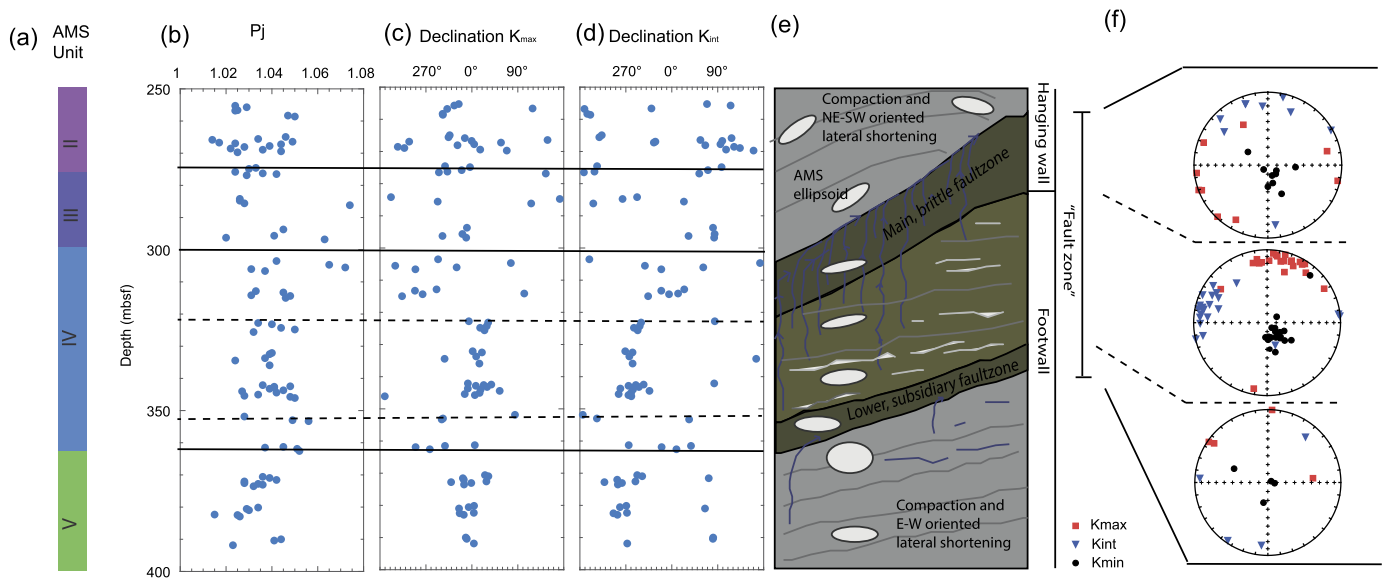
and visibly deformed fold hinge zone in the hanging wall (section 4.2.1), (iii) a clear correlation between different AMS shape ellipsoids and the main structural domains, (iv) a decrease of the corrected anisotropy degree Pj at the top of AMS Unit V, which is coherent with a sharp increase in porosity at the same depth.

During the interpretation of the magnetic fabrics one needs to keep in mind that the contribution of differing ferro- and paramagnetic mineral phases to the AMS ellipsoids is not fully known. A clay mineral content of 45% and the overall small difference between the high-field and bulk magnetic susceptibility measured indicate that the alignment of paramagnetic clay minerals, dominate the shape of the AMS ellipsoids measured. It is likely that the ferromagnetic minerals, such as greigite enhance or counteract the fabric produced by the clay minerals. Their to-

**Fig. 5.** Downhole variations in (a) AMS units, (b) the corrected degree of anisotropy Pj, (c) the declination of $K_{max}$, (d) the declination of $K_{int}$ in core-coordinates and (f) the distribution of the three principal axes of magnetic susceptibility for the upper strand of the Pāpaku fault zone between 304.5 and 322.4 mbsf, the center of the fault zone between 322.4 and 351.2 mbsf, and the lower strand of the Pāpaku fault zone between 351.2 and 361.7 mbsf. (e) Conceptual model of fault zone deformation and dewatering discussed in this paper.

The orientation of the principal strain direction in the footwall is thus oblique to the strain ellipsoid inferred from the AMS measurements within the hanging wall sequence and the main brittle fault zone. We propose that the sediment fabrics formed in response to the partitioning of oblique and margin parallel plate motions. Paleomagnetic directions were used to determine the axial orientation of the samples, and the distribution of the principal axes of susceptibility is thus likely to reflect a combination of strain and vertical axis rotations. East of New Zealand, the relative motion of the Pacific Plate in respect to the Australian Plate is southwest and thus oblique to the trench (e.g. Townend et al., 2012; Barnes et al., 1998). At the drill-site the Pacific Plate is subducting roughly in W direction beneath the Australian Plate (Wallace et al., 2004, 2019). The margin parallel (N-S) motion is thought to be largely accommodated by dextral strike-slip faulting within the overriding Australian plate (e.g. Beanland et al., 1998). This interpretation is supported by the GPS velocity field (e.g. Wallace et al., 2004), focal mechanisms on the plate interface (Townend et al., 2012; Webb and Anderson, 1998) and structural mapping on-shore (e.g. Beanland et al., 1998). Furthermore, borehole breakouts in the footwall of Site U1518 at depths > 500 mbsf are elongated N-S which indicates that the present-day maximum horizontal stress within the lower accretionary system is also oriented E-W (Wallace et al., 2019). At the drill-site, the underthrust footwall yields magnetic deformation ellipsoids that reflect the prevalent convergence vector (E-W) of the subducting Pacific Plate. In contrast, lateral shortening of the sediments in the hanging wall is oblique to the margin and accommodates, in effect, transcurrent strain of the overriding Australian Plate. Because in this setting the footwall is located within the accretionary system, these results provide unequivocal evidence for the decoupling of margin parallel and oblique strain components along the shallow thrust fault and during evolution of the accretionary prism. Because it is difficult or impossible to unravel strain histories based on unoriented drill-cores, little information is available to-date on the strain distribution across young subduction thrust faults. Hence, our results may significantly further our understanding of the development of young accretionary prisms.

## 5.2. Strain variation across the Pāpaku fault zone, their implications for sediment dewatering and pore-fluid distribution

Pore fluids, their migration pathways and pressure distribution are known to have a major impact on the formation of sedimentary fabric, the architecture and the frictional stability of fault zones (e.g. Skarbek and Saffer, 2009; Saffer, 2015). In active accretionary margins where porous, water-rich sediments are compacted it is thought to have a major impact on the slip behavior (e.g. Morgan and Karig, 1995; Moore and Vrolijk, 1992; Skarbek and Saffer, 2009; Saffer, 2015). Localized zones of sediment fluidization within the Pāpaku fault zone (Fagereng et al., 2019) indicate that the pore-fluid pressure across the fault zone is high. This indicates that the dewatering of the sediments during compaction and tectonic fabric development plays an important role in the evolution of the fault zone. Trapped fluids in clay-rich sediments hamper the collapse of pore-space and shape preferred orientation of the grains (see for example Yang et al., 2013; Morgan and Karig, 1995; Skarbek and Saffer, 2009; Housen et al., 1996; Parés, 2015). The degree of magnetic anisotropy developed by sediments in and beneath décollement zones is thus directly linked to the distribution of pore fluids (see for example Yang et al., 2013).

As discussed in section 5.1, the change in shape and orientation of the AMS ellipsoids occurs abruptly at the top of the upper main brittle fault zone (Figs. 4, 5), which provides evidence for the fact that this fault zone acts as a decoupling horizon. The orientation of the principal axes of magnetic susceptibility within the upper main brittle fault zone depicts a significantly different deformation regime within this zone than the over- and underlying sequences. In contrast, samples from the less pervasively and ductilely deformed remainder of the fault zone (~322.4-361.7 mbsf) display similar magnetic shape ellipsoids as the footwall sequence. This observation supports interpretations of Fagereng et al. (2019), which suggest that the central part of the fault zone is part of the footwall sequence and thus experienced a similar strain history, prior to faulting. Remarkably however, the porosity and corrected degree of anisotropy (Pj) throughout the fault zone remain largely consistent with the hanging wall. A small decrease in Pj in the upper footwall coincides with an increase in porosity (Fig. 2c).

Numerous authors (e.g. Morgan and Karig, 1995; Skarbek and Saffer, 2009; Housen et al., 1996) discussed the importance of brittle structures as fluid conduits in clay-rich sediments. We propose that in this setting, the upper main brittle fault zone acts as a primary conduit for the pore-fluids released during underthrusting and underplating (Fig. 5e). This allows drainage and essentially the fabric development within the central "weakly deformed" part of the fault zone that exceeds the one of the footwall sequences beneath. Elevated fluid pressure within the upper strand of the Pāpaku fault likely contributes to the decoupling of strain between hanging- and footwall.

Limited sample material does not allow us to draw conclusions about the predominant compressive shortening direction within the subsidiary fault zone, i.e., whether the predominant principal strain direction differs from the footwall. Nevertheless, shipboard core descriptions found that this fault zone is dominated by ductile deformation features with fewer brittle structures than what is present within the main fault zone (Wallace et al., 2019). This indicates lower permeability through the subsidiary fault zone, and thus reduces dewatering and fabric development in the footwall beneath. The upper footwall can thus be seen as a precursor to the central segment of the fault zone, where dewatering has further progressed. This spatial difference in clay-mineral fabric and permeability likely results in differing frictional stability between the two strands of the fault zone.

## 6. Conclusions

The AMS datasets presented in this paper allow to characterize the mineral texture and thus the distribution of strain in soft sediments recovered at IODP Site U1518. The site penetrated the Pāpaku fault, a major splay fault near the deformation front of the Hikurangi subduction margin, New Zealand. The Pāpaku fault encompasses a roughly 60 m thick and variably deformed fault zone in which the majority of strain is localized within two major strands, here referred to as the upper brittle, and lower subsidiary fault zones. The AMS results presented in this paper display a clear correlation between AMS and the main structural domains, including hanging wall, fault zone and footwall sequences. Hanging wall sequences are dominated by a bedding-parallel foliation with a variable degree of superimposed horizontal strain in NE-SW direction. In contrast, the footwall sequences depict a significantly different deformation regime in which $K_{max}$ forms a cluster in N direction, which is indicative for weak E-W oriented lateral shortening. We propose that this distribution reflects the partitioning of margin parallel and oblique strain components. The AMS fabric changes abruptly at the top of the main brittle fault zone, suggesting that it acts as a decoupling horizon which is enhanced by the migration of fluids that are released by the compaction of the porous and water-rich footwall sediments within the fault zone and beneath.

## Declaration of competing interest

The authors declare that they have no known competing financial interests or personal relationships that could have appeared to influence the work reported in this paper.

## Acknowledgements

## Appendix A. Supplementary material

Supplementary material related to this article can be found online at https://doi.org/10.1016/j.epsl.2020.116322.

## References

Aubourg, C., Robion, P., 2002. Composite ferromagnetic fabrics (magnetite, greigite) measured by AMS and partial AARM in weakly strained sandstones from western Makran, Iran. Geophys. J. Int. 151 (3), 729–737. https://doi.org/10.1046/j.1365-246X.2002.01800.x.

Barker, D.H.N., Henrys, S., Caratori Tontini, F., Barnes, P.M., Bassett, D., Todd, E., Wallace, L., 2018. Geophysical constraints on the relationship between seamount subduction, slow slip, and tremor at the North Hikurangi Subduction Zone, New Zealand. Geophys. Res. Lett. 45 (23), 12,804–12,813. https://doi.org/10.1029/2018gl080259.

Barnes, P.M., de Lépinay, B.M., Collot, J.-Y., Delteil, J., Audru, J.-C., 1998. Strain partitioning in the transition area between oblique subduction and continental collision, Hikurangi margin, New Zealand. Tectonics 17 (4), 534–557. https://doi.org/10.1029/98TC00974.

Beanland, S., Melhuish, A., Nicol, A., Ravens, J., 1998. Structure and deformational history of the inner forearc region, Hikurangi subduction margin, New Zealand. N.Z. J. Geol. Geophys. 41 (4), 325–342. https://doi.org/10.1080/00288306.1998.9514814.

Bell, R., Holden, C., Power, W., Wang, X., Downes, G., 2014. Hikurangi margin tsunami earthquake generated by slow seismic rupture over a subducted seamount. Earth Planet. Sci. Lett. 397, 1–9. https://doi.org/10.1016/j.epsl.2014.04.005.

Cifelli, F., Mattei, M., Hirt, A.M., Günther, A., 2004. The origin of tectonic fabrics in "undeformed" clays: the early stages of deformation in extensional sedimentary basins. Geophys. Res. Lett. 31 (9). https://doi.org/10.1029/2004gl019609.

Fagereng, Å., Savage, H.M., Morgan, J.K., Wang, M., Meneghini, F., Barnes, P.M., Barnes, P.M., Bell, R., Kitajima, H., McNamara, D.D., Saffer, D.M., Wallace, L.M., Petronotis, K., LeVay, L., IODP Expedition 372/375 Scientists, 2019. Mixed deformation styles observed on a shallow subduction thrust, Hikurangi margin, New Zealand. Geology 47, 872–876. https://doi.org/10.1130/G46367.1.

Graham, J.W., 1966. Significance of magnetic anisotropy in Appalachian sedimentary rocks. In: Steinhart, J.S., Smith, T.J. (Eds.), The Earth Beneath the Continents. In: Geophysical Monograph, vol. 10. American Geophysical Union, Washington, pp. 627–648.

Greve, A., Turner, G.M., 2017. New and revised palaeomagnetic secular variation (PSV) records from postglacial volcanic materials in New Zealand. Phys. Earth Planet. Inter. 269, 1–17. https://doi.org/10.1016/j.pepi.2017.05.009.

Harrison, R.J., Feinberg, J., 2008. FORCInel: an improved algorithm for calculating first order reversal curve distributions using locally weighted regression smoothing. Geochem. Geophys. Geosyst. 9 (Q05016). https://doi.org/10.1029/2008GC001987.

Hirt, A.M., Lowrie, W., Lüneburg, C., Lebit, H., Engelder, T., 2004. Magnetic and mineral fabric development in the Ordovician Martinsburg Formation in the Central Appalachian Fold and Thrust Belt, Pennsylvania. Geol. Soc. (Lond.) Spec. Publ. 238 (1), 109. https://doi.org/10.1144/GSL.SP.2004.238.01.09.

Housen, B.A., Kanamatsu, T., 2003. Magnetic fabrics from the Costa Rica margin: sediment deformation during the initial dewatering and underplating process. Earth Planet. Sci. Lett. 206 (1), 215–228. https://doi.org/10.1016/S0012-821X(02)01076-2.

Housen, B.A., Tobin, H.J., Labaume, P., Leitch, E.C., Maltman, A.J., Ocean Drilling Program Leg 156 Shipboard Science Party, 1996. Strain decoupling across the decollement of the Barbados accretionary prism. Geology 24 (2), 127–130. https://doi.org/10.1130/0091-7613(1996)024<0127:sdatdo>2.3.co;2.

Hu, S., Stephenson, A., Appel, E., 2002. A study of gyroremanent magnetisation (GRM) and rotational remanent magnetisation (RRM) carried by greigite from lake sediments. Geophysical Journal International 151 (2), 469–474. https://doi-org.proxy.library.uu.nl/10.1046/j.1365-246X.2002.01793.x.

Jelinek, V., 1981. Characterization of the magnetic fabric of rocks. Tectonophysics 79, T63–T67. https://doi.org/10.1016/00401951(81)90110-4.

Kanamatsu, T., Herrero-Bervera, E., Taira, A., 2001. Magnetic fabrics of soft-sediment folded strata within a Neogene accretionary complex, the Miura group, central Japan. Earth Planet. Sci. Lett. 187 (3), 333–343. https://doi.org/10.1016/S0012-821X(01)00292-8.

Kanamatsu, T., Herrero-Bervera, E., Taira, A., Saito, S., Ashi, J., Furumoto, A.S., 1996. Magnetic fabric development in the Tertiary Accretionary Complex in the Boso and Miura Peninsulas of central Japan. Geophys. Res. Lett. 23 (5), 471–474. https://doi.org/10.1029/96GL00147.

Kanamatsu, T., Parés, J.M., Kitamura, Y., 2012. Pliocene shortening direction in Nankai Trough off Kumano, southwest Japan, Sites IODP C0001 and C0002, Expedition 315: Anisotropy of magnetic susceptibility analysis for paleostress. Geochem. Geophys. Geosyst. 13 (1). https://doi.org/10.1029/2011GC003782.

Kars, M., Greve, A., Zerbst, L., 2019. Occurrence of Greigite in Gas Hydrate-bearing Frontal Thrust Sediments of the Hikurangi Margin, New Zealand at Site U1518, IODP Expedition 375. Abstract GP21A-08 presented at the 2019 AGU Fall Meeting, San Francisco.

Kitamura, Y., Kanamatsu, T., Zhao, X., 2010. Structural evolution in accretionary prism toe revealed by magnetic fabric analysis from IODP NanTroSEIZE Expedition 316. Earth Planet. Sci. Lett. 292 (1), 221–230. https://doi.org/10.1016/j.epsl.2010.01.040.

Kuehn, R., Hirt, A.M., Biedermann, A.R., Leiss, B., 2019a. Quantitative comparison of microfabric and magnetic fabric in black shales from the Appalachian plateau (western Pennsylvania, U.S.A.). Tectonophysics 765, 161–171. https://doi.org/10.1016/j.tecto.2019.04.013.

Kuehn, R., Stipp, M., Leiss, B., 2019b. Texture development of clay-rich sediments across the Costa Rica subduction zone. J. Geophys. Res., Solid Earth 124, 7756–7770. https://doi.org/10.1029/2018JB016838.

Moore, G.F., Saffer, D., Studer, M., Costa Pisani, P., 2011. Structural restoration of thrusts at the toe of the Nankai Trough accretionary prism off Shikoku Island, Japan: implications for dewatering processes. Geochem. Geophys. Geosyst. 12 (5). https://doi.org/10.1029/2010GC003453.

Moore, J.C., Vrolijk, P., 1992. Fluids in accretionary prisms. Rev. Geophys. 30 (2), 113–135. https://doi.org/10.1029/92RG00201.

Morgan, J.K., Karig, D.E., 1995. Décollement processes at the Nankai accretionary margin, southeast Japan: propagation, deformation, and dewatering. J. Geophys. Res., Solid Earth 100 (B8), 15221–15231. https://doi.org/10.1029/95jb00675.

Morgan, J.K., Ramsey, E.B., Ask, M.V.S., 2007. Deformation and mechanical strength of sediments at the Nankai Subduction Zone. In: Dixon, T.H., Casey, J. (Eds.), The Seismogenic Zone of Subduction Thrust Faults. Columbia University Press, New York, pp. 210–256.

Muxworthy, A.R., Dunlop, D.J., 2002. First-order reversal curve (FORC) diagrams for pseudosingle-domain magnetites at high temperature. Earth Planet. Sci. Lett. 203, 369–382.

Novak, B., Housen, B., Kitamura, Y., Kanamatsu, T., Kawamura, K., 2014. Magnetic fabric analyses as a method for determining sediment transport and deposition in deep sea sediments. Mar. Geol. 356, 19–30. https://doi.org/10.1016/j.margeo.2013.12.001.

Owens, W., 1993. Magnetic fabric studies of samples from hole 808C, Nankai Trough. Proc. Ocean Drill. Program Sci. Results 131, 301–310. https://doi.org/10.2973/odp.proc.sr.131.130.1993.

Parés, J.M., 2015. Sixty years of anisotropy of magnetic susceptibility in deformed sedimentary rocks. Front. Earth Sci. 3. https://doi.org/10.3389/feart.2015.00004.

Pike, C.R., Roberts, A.P., Verosub, K.L., 1999. Characterizing interactions in fine magnetic particle systems using first order reversal curves. J. Appl. Phys. 85 (9), 6660–6667. https://doi.org/10.1063/1.370176.

Roberts, A.P., Pike, C.P., Verosub, K.L., 2000. First-order reversal curve diagrams: A new tool for characterizing the magnetic properties of natural samples. J. Geophys. Res. 105 (B12), 28461–28475. https://doi.org/10.1029/2000JB900326.

Roberts, A.P., Liu, Q., Rowan, C.J., Chang, L., Carvallo, C., Torrent, J., Horng, C.-S., 2006. Characterization of hematite (a-Fe2O3), goethite (a-FeOOH), greigite (Fe3S4), and pyrrhotite (Fe7S8) using first-order reversal curve diagrams. J. Geophys. Res. 111 (B12S35). https://doi.org/10.1029/2006JB004715.

Saffer, D.M., 2015. The permeability of active subduction plate boundary faults. Geofluids 15 (1–2), 193–215. https://doi.org/10.1111/gfl.12103.

Skarbek, R.M., Saffer, D.M., 2009. Pore pressure development beneath the décollement at the Nankai subduction zone: implications for plate boundary fault strength and sediment dewatering. J. Geophys. Res., Solid Earth 114 (B7). https://doi.org/10.1029/2008jb006205.

Snowball, I., Almqvist, B., Lougheed, B.C., Wiers, S., Obrochta, S., Herrero-Bervera, E., 2019. Coring induced sediment fabrics at IODP Expedition 347 Sites M0061 and M0062 identified by anisotropy of magnetic susceptibility (AMS): criteria for accepting palaeomagnetic data. Geophys. J. Int. 217 (2), 1089–1107. https://doi.org/10.1093/gji/ggz075.

Stipp, M., Rolfs, M., Kitamura, Y., Behrmann, J.H., Schumann, K., Schulte-Kortnack, D., Feeser, V., 2013. Strong sediments at the deformation front, and weak sediments at the rear of the Nankai accretionary prism, revealed by triaxial deformation experiments. Geochem. Geophys. Geosyst. 14 (11), 4791–4810. https://doi.org/10.1002/ggge.20290.

Taira, A., Hill, I., Firth, J., Berner, U., Brückmann, W., Byrne, T., Chabernaud, T., Fisher, A., Foucher, J.P., Gamo, T., Gieskes, J., Hyndman, R., Karig, D., Kastner, M., Kato, Y., Lallemant, S., Lu, R., Maltman, A., Moore, G., Moran, K., Olaffson, G., Owens, W., Pickering, K., Siena, F., Taylor, E., Underwood, M., Wilkinson, C., Yamano, M., Zhang, J., 1992. Sediment deformation and hydrogeology of the Nankai Trough accretionary prism: Synthesis of shipboard results of ODP Leg 131. Earth Planet. Sci. Lett. 109 (3), 431–450. https://doi.org/10.1016/0012-821X(92)90104-4.

Townend, J., Sherburn, S., Arnold, R., Boese, C., Woods, L., 2012. Three-dimensional variations in present-day tectonic stress along the Australia–Pacific plate boundary in New Zealand. Earth Planet. Sci. Lett. 353–354, 47–59. https://doi.org/10.1016/j.epsl.2012.08.003.

Ujiie, K., Hisamitsu, T., Taira, A., 2003. Deformation and fluid pressure variation during initiation and evolution of the plate boundary décollement zone in the Nankai accretionary prism. J. Geophys. Res. 108 (B8). https://doi.org/10.1029/2002JB002314.

Wallace, L.M., Beavan, J., McCaffrey, R., Darby, D., 2004. Subduction zone coupling and tectonic block rotations in the North Island, New Zealand. J. Geophys. Res., Solid Earth 109 (B12). https://doi.org/10.1029/2004JB003241.

Wallace, L.M., Saffer, D.M., Barnes, P.M., Pecher, I.A., Petronotis, K.E., LeVay, L.J., Scientists, E., 2019. Proc. Int. Ocean Discov. Program 372B/375. https://doi.org/10.14379/iodp.proc.372B375.103.2019.

Wallace, L.M., Webb, S.C., Ito, Y., Mochizuki, K., Hino, R., Henrys, S., Schwartz, S., Sheehan, A.F., 2016. Slow slip near the trench at the Hikurangi subduction zone, New Zealand. Science 352 (6286), 701–704. https://doi.org/10.1126/science.aaf2349.

Webb, T.H., Anderson, H., 1998. Focal mechanisms of large earthquakes in the North Island of New Zealand: slip partitioning at an oblique active margin. Geophys. J. Int. 134 (1), 40–86. https://doi.org/10.1046/j.1365-246x.1998.00531.x.

Yang, T., Mishima, T., Ujiie, K., Chester, F.M., Mori, J.J., Eguchi, N., Toczko, S., 2013. Strain decoupling across the décollement in the region of large slip during the 2011 Tohoku-Oki earthquake from anisotropy of magnetic susceptibility. Earth Planet. Sci. Lett. 381, 31–38. https://doi.org/10.1016/j.epsl.2013.08.045.